JM PAPERS

Melting processes of phase change materials in a horizontally placed rectangular cavity

Min Li[1], Zhenjun Jiao[1] and Pan Jia[1],†

[1] School of Science, Harbin Institute of Technology, Shenzhen 518055, PR China

This paper revisits the melting process of phase change materials (PCMs) enclosed in a horizontally placed rectangular cavity, with isothermal and adiabatic conditions subjected to the vertical and horizontal walls, respectively. First, numerical simulations based on an improved lattice Boltzmann method are conducted to illustrate and to inform the theoretical modelling. It is shown that, compared with the traditional two-stage conduction–convection melting description, it is more reasonable to include a third stage in terms of the heat transfer behaviour. During the third stage, the remnant solid PCM is located in the corner formed by the cold and bottom walls of the cavity, and an increasing part of the input energy will be transferred directly out of the cavity without compensating for the melting latent heat, thus inducing a continuously decreasing melting rate until the end of the melting process. Then theoretical predictions are derived piecewise for the melted liquid fraction during the entire melting process, and the corresponding transitions between two successive stages are also discussed. The results are validated successfully via the available experimental and numerical data in the literature, and could guide the design and operation of latent heat storage systems.

Key words: solidification/melting, convection in cavities

1. Introduction

Solid–liquid phase change and the accompanying thermal flows remain an active research area, being ubiquitous in geophysical and industrial processes, such as the evolution of ice crust (Z. Wang, Calzavarini & Sun 2021*a*; Wang *et al.* 2021*b*,*d*), the formation of the Earth's inner core (Alboussiere, Deguen & Melzani 2010), and particularly, thermal energy storage (Wang, Faghri & Bergman 2010). The last of the listed examples has drawn considerable attention due to the ever-growing global energy issues and the consequent environmental problems, encouraging researchers from different fields to explore new energy storage technologies. Thus far, thermal energy is usually stored in

† Email address for correspondence: jiapan@hit.edu.cn

three ways: sensible heat, latent heat performed by phase change materials (PCMs), and thermo-chemical heat. Comparatively speaking, the highest storage density is observed in thermo-chemical heat, but its operating temperature range is generally the narrowest, limiting its commercial viability (Nazir *et al.* 2019). For the two other ways, the storage density of latent heat is generally 5–14 times higher than that of sensible heat (Garg, Mullick & Bhargava 2012). Meanwhile, the latent heat storage technique shows the most flexible operating temperature range because many types of PCMs are available for selection. Each type of PCM generally presents a unique and almost constant operating temperature (melting point), thereby resulting in nearly isothermal charging and discharging processes (Sharma *et al.* 2009; Dutil *et al.* 2011; Zhou, Zhao & Tian 2012; Shokouhmand & Kamkari 2013; Dhaidan & Khodadadi 2015). These favourable properties contributed to the promising applications of PCMs in various situations, including electronics cooling (Baby & Balaji 2013; Levin, Shitzer & Hetsroni 2013), thermal comfort in buildings (Lee *et al.* 2015; Ramakrishnan *et al.* 2016), thermal protection of spacecraft (Swanson & Birur 2003; Kim *et al.* 2013) and smart textiles (Sarier & Onder 2012). The consistently growing interest in PCMs has currently stimulated massive investigation efforts on their melting processes, which aim mainly to predict the melting rate, defined as the time derivative of the melted liquid fraction f_l. The melting rate is closely related to thermal flow dynamics; thus this rate is one of the most important parameters in fundamental scientific understanding (Esfahani *et al.* 2018). The melting rate also determines the energy storage efficiency, therefore being a key factor to consider in engineering applications (Hannoun, Alexiades & Mai 2003).

The melting of PCMs is governed by conservation laws of mass, momentum and energy. Normalising the melting system, the following four dimensionless control parameters are generally deduced: the Rayleigh number Ra, the Prandtl number Pr, the Stefan number Ste, and the aspect ratio of the cavity γ, which have been studied extensively (Bertrand *et al.* 1999; Huang, Wu & Cheng 2013; Li, Yang & Zhang 2014; Esfahani *et al.* 2018; Hasan & Saha 2021). Rayleigh number Ra weighs the relative intensity of convection over diffusion, influencing significantly the melting interface morphology and the melting rate (Ho & Viskanta 1984; Gau & Viskanta 1985; Wang, Amiri & Vafai 1999; Shokouhmand & Kamkari 2013). A small Pr lengthens the conduction stage, and alleviates the convection effect on the interface morphology and melting rate (Webb & Viskanta 1986; Wolff & Viskanta 1988). A large Ste would delay the onset of convection, indicating that the melting of PCMs is energetically inexpensive (Kim, Lee & Choi 2008; Esfahani *et al.* 2018). In addition to the Stefan number, γ also affects the onset of convection (Gadgil & Gobin 1984; El Qarnia, Draoui & Lakhal 2013; Behbahan *et al.* 2019). Hamad *et al.* (2021) found recently that an earlier transition from conduction to convection will be observed during the PCM melting, when the width of a rectangular container is increased. It is seen clearly that all these control parameters influence the melting rate. Thus developing a prediction, including all their effects, is necessary. In addition to the four dimensionless numbers, the melting rate also depends on the cavity shape (cylinder, sphere, rectangular, etc.) (Bareiss & Beer 1984; Dhaidan & Khodadadi 2015), inclination angle (Baby & Balaji 2013; Sharifi *et al.* 2013; Kamkari, Shokouhmand & Bruno 2014; Yang *et al.* 2019) and thermal boundary conditions, such as uniform or partial heating with constant heat flux or temperature (Zhang *et al.* 1993; Gong, Devahastin & Mujumdar 1999; Jourabian, Farhadi & Darzi 2013; Rui *et al.* 2020).

Amongst various PCM melting configurations, the most frequently employed one is a rectangular cavity placed horizontally and heated uniformly on a vertical wall (figure 1). A considerable amount of research has been conducted experimentally or numerically for
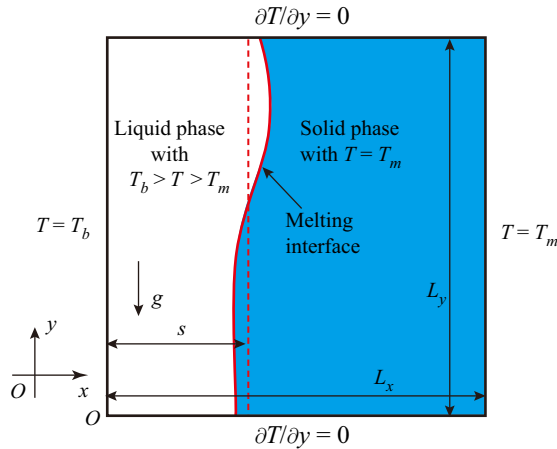
Figure 1. Schematic of PCM melting in a rectangular cavity, and the boundary conditions. The origin of coordinates O lies in the bottom left corner.

this configuration, to explore the effect of dimensionless control parameters on melting behaviours. The investigated PCMs cover from low Pr metals (Gau & Viskanta 1986; Webb & Viskanta 1986; Wolff & Viskanta 1988; Campbell & Koster 1994; Bertrand *et al.* 1999) to medium Pr water (Boger & Westwater 1967) and high Pr materials, such as paraffins (Bareiss & Beer 1984; Ho & Viskanta 1984; Bénard, Gobin & Martinez 1985; Bertrand *et al.* 1999; Kadri *et al.* 2015; Faden *et al.* 2019), fatty acids (Shokouhmand & Kamkari 2013; Kamkari *et al.* 2014) and polyethylene glycol (PEG) (Wang *et al.* 1999; Ahmad *et al.* 2006; Hamad *et al.* 2017, 2021). Amongst these studies, several fitting expressions, usually termed 'correlations', are reported for the melted liquid fraction f_l, as summarised in table 1.

The first correlation was reported by Ho & Viskanta (1984), in which f_l depends on a combination of the dimensionless control numbers as $Ra^{0.25}\, Ste\, Fo_x\, \gamma^2$ for *n*-octadecane (table 1, row 1). In this expression, $Fo_x = \alpha t/L_x^2$ is the Fourier number, i.e. the dimensionless time based on the thermal diffusivity α and the horizontal dimension of the rectangular cavity L_x. A similar dependence was reported later by Bénard *et al.* (1985) for the same material (table 1, row 2). However, the reported dependencies (table 1, rows 1 and 2) were found to be insufficient to achieve data regression for the experimental measurements on gallium melting as performed by Gau & Viskanta (1986), which has been used widely to test numerical models and other experiments (Kadri *et al.* 2015). Therefore, instead of using the $Ra^{0.25}\, Ste\, Fo_x\, \gamma^2$ combination, Gau & Viskanta (1986) considered Ste, Fo_x, Ra and γ as individual independent variables, and reported a different correlation (table 1, row 3), where a $\gamma^{0.14}$ dependence was found. Meanwhile, a second correlation, which also fits well on the experimental data, was obtained by replacing Ra with Ste (table 1, row 3). In this correlation, a remarkably weak and opposite dependence on the aspect ratio was $\gamma^{-0.0137}$, which is inconsistent with the first correlation. Subsequently, a similar experiment conducted by Wolff & Viskanta (1988) with tin indicates that Ra plays an important role in the melting process due to its generally high value ($9.0 \times 10^4 \le Ra \le 2.1 \times 10^5$), despite the weak dependence in the correlation (table 1, row 4). This finding indicates that the first correlation by Gau & Viskanta (1986) is more reasonable than the second correlation, to some extent. However, the γ dependence is opposite. In the same year, Jany & Bejan (1988) proposed numerically another correlation (table 1, row 5) in a quite different form, in which a parameter combination $Ste\, Fo_x\, \gamma^2$ was employed.

950 A34-3

No.	Literature	Correlations for f_l	Conditions
1	Ho & Viskanta (1984)	$f_l = 0.523(Ra^{0.25}\, Ste\, Fo_x\, \gamma^2)^{0.68}$	$6.3 \times 10^7 \le Ra \le 1.4 \times 10^8$ $0.063 \le Ste \le 0.132$ $\gamma = 0.3846,\, Pr = 56$ PCM: n-octadecane
2	Bénard *et al.* (1985)	$f_l = \begin{cases}(t^+ + t_0^+)/\gamma, \\ 1 - y_D(1 - 2\tau_0) + (\tau - \tau_0)I(y_D),\end{cases}$ with $t^+ = 0.33\, Ra^{0.25}\, \rho^+\, Ste\, Fo_x\, \gamma^2$, $t_0^+ = Ra^{0.25}/0.66,\ \tau = t^+/\gamma$, ρ^+ the liquid–solid density ratio, y_D the interface–wall intercept, and $I(y_D)$ the integration	$Ra = 1.09 \times 10^9,\, Ste = 0.084$ $\gamma = 0.3876,\, Pr = 50.9$ PCM: n-octadecane
3	Gau & Viskanta (1986)	(1) $f_l = 2.71(Ste\, Fo_x)^{0.84}\, Ra^{0.05}\, \gamma^{0.14}$ (2) $f_l = 6.28(Ste\, Fo_x)^{0.84}\, Ste^{0.04}\gamma^{-0.0137}$	$3.4 \times 10^4 \le Ra \le 6.1 \times 10^5$ $0.009 \le Ste \le 0.083$ $1.40 \le \gamma \le 3.50$ $Pr = 0.0216$ PCM: gallium
4	Wolff & Viskanta (1988)	$f_l = 1.23(Ste\, Fo_x)^{0.56}\, Ra^{0.02}\, \gamma^{-0.09}$	$9.0 \times 10^4 \le Ra \le 2.1 \times 10^5$ $0.0047 \le Ste \le 0.011$ $\gamma = 1.0,\, 1.33$ $Pr = 0.0157$ PCM: tin
5	Jany & Bejan (1988)	$f_l = [(\sqrt{2\zeta})^5 + (0.27\zeta\, Ra^{1/4})^5]^{1/5}$, with $\zeta = Fo_x\, Ste\, \gamma^2$	$0 \le Ra \le 10^8,\, Ste = 0.1$ $\gamma = 1.0,\, Pr = 50$ PCM: n-octadecane
6	Wang *et al.* (1999)	$f_l = 4.73\, Fo_x^{0.91}\, Ste^{1.54}\, Ra^{0.002}$	$2.0 \times 10^6 \le Ra \le 2.6 \times 10^7$ $0.081 \le Ste \le 0.41$ $\gamma = 1.4854$ $804 \le Pr \le 1055$ PCM: PEG900
7	Du *et al.* (2007)	$f_l = 0.23(Fo_x\, \gamma^2)^{0.702}\, Ste^{0.51}\, Ra^{0.258}$	$1.5 \times 10^7 \le Ra \le 4.0 \times 10^9$ $0.04 \le Ste \le 0.3$ $\gamma \le 0.179,\, Pr = 693$ PCM: MEA–water mixture
8	Duan, Xiong & Yang (2019)	$f_l = -0.39(X^3 - X^2) + 0.92X$, with $X = \dfrac{[((1.57\zeta)^{0.52})^{3.5} + (0.22\zeta\, Ra^{0.25})^{3.5}]^{1/3.5}}{\gamma}$	$4.0 \times 10^4 \le Ra \le 6.9 \times 10^5$ $Ste = 0.46,\, 0.3 \le \gamma \le 2.0$ $Pr = 6.72$ PCM: water–ice

Table 1. Summary of the reported correlations for the melted liquid fraction f_l in the literature. Note that the definitions of dimensionless numbers are already unified in this table, as given in (2.6*a–d*) and (2.7*a,b*) in § 2.

However, the reported correlation leads to a substantial overestimation (Duan *et al.* 2019). More than 10 years later, Wang *et al.* (1999) revisited the melting experiment with high *Pr* material PEG900 and reported a correlation (table 1, row 6). Compared with the first correlation by Gau & Viskanta (1986), the authors found a similar dependence on Fo_x yet a quite different one on *Ste*. Moreover, this correlation does not include the effect of γ. Du *et al.* (2007) investigated experimentally the melting process of ethanolamine (MEA)–water binary mixture, and reported a correlation for the melted liquid fraction f_l (table 1, row 7). In this correlation, the dependencies on Fo_x and γ are very close to those in the first correlation by Gau & Viskanta (1986). However, a major discrepancy exists

in *Ra* dependence. Recently, Duan *et al.* (2019) investigated numerically the water–ice melting process and obtained a third-order polynomial correlation (table 1, row 8), which is substantially different from the existing correlations. Overall, the existing correlations obtained from different or even the same studies are incompatible, and none of these correlations includes the effect of *Pr*. Thus, on the basis of the existing data, obtaining a general solution for the melted liquid fraction f_l by an experimental or numerical fit is almost impossible. Thus theoretical explorations starting from the governing equations of the melting process are inevitable.

When it comes to the theoretical modelling, PCM melting includes a strong nonlinear interaction between the evolving melting interface and convection. Therefore, only the simplest one-dimensional infinite or semi-infinite configuration can be solved analytically (Hamdan & Elwerr 1996; Hannoun *et al.* 2003; Hamdan & Al-Hinti 2004; Dutil *et al.* 2011; Kadri *et al.* 2015; Rui *et al.* 2020). For the two-dimensional (2-D) and three-dimensional (3-D) geometric configurations, the melting system is analytically accessible only under some simplifications. For the rectangle configuration emphasised in the present paper, Hamdan & Elwerr (1996) simplified the melting interface as an inclined plane, and the local melting layer thickness was assumed to be $S(y) = S_0 + y\tan(\phi)$. In the assumption, S_0 is the local thickness of the liquid PCM at the bottom wall, where the melting is considered to be dominated by conduction. Angle ϕ is the inclination angle of the interface, and is estimated by trial and error based on a nonlinear equation. Obviously, although the melting interface is simplified and described by two parameters (S_0 and ϕ), its expression and that of the melted liquid fraction f_l cannot be provided explicitly due to the estimation of ϕ. Moreover, the predicted f_l deviates from that of Webb & Viskanta (1986) despite its agreement with the measurements of Bénard *et al.* (1985). This deviation is because the interface inclination angle was calibrated by the experimental data of Bénard *et al.* (1985), which, however, cannot be generalised, as previously mentioned. Thus the analytical attempts for 2-D and 3-D PCM melting models remain to be pushed forward, in order to develop a feasible and universal prediction for the melted liquid fraction f_l, and its melting rate.

This paper is devoted to the theoretical prediction of the melting process in a rectangle PCM melting system. Numerical simulations based on an improved lattice Boltzmann method are performed to illustrate and to inform the derivations, and available data in the literature are employed to validate the prediction. The remainder of the paper is organised as follows. Section 2 first presents the equations governing the melting process and provides some brief information regarding the involved numerical simulations. A comparison between pure thermal flows without phase change and melting thermal flows is also presented to offer a deep insight into the melting processes. Section 3 derives and verifies the theoretical predictions for the entire melting process. Section 4 introduces the discussions on the distorted melting interface, parameter space, 3-D effect and transitions between two successive melting stages. Section 5 concludes the paper.

2. Thermal flows

2.1. *Governing equations*

As shown in figure 1, the most frequently employed configuration in the PCM melting cases is considered. In the figure, a 2-D horizontally placed rectangular cavity is filled with a block of pure solid PCM, presenting a uniform bulk temperature T_m at its melting point. The left wall temperature is raised to $T_b > T_m$ at some point, but that of the right wall is maintained at T_m; two horizontal walls are adiabatic. The solid PCM near the

left wall then will melt into liquid, and thermal convection will be induced eventually and driven by buoyancy. A laminar incompressible Newtonian fluid flow is assumed for thermal convection as in previous studies, which effectively predicted the PCM melting process (Webb & Viskanta 1986; Brent, Voller & Reid 1988; Chakraborty & Chatterjee 2007; Huang *et al.* 2013; Luo *et al.* 2015; Duan *et al.* 2019). In this case, the equations governing the velocity field $\boldsymbol{u}$ and the pressure p inside the melted liquid can be written respectively as

$$\nabla \cdot \boldsymbol{u} = 0, \tag{2.1}$$

$$\rho \left(\frac{\partial \boldsymbol{u}}{\partial t} + \boldsymbol{u} \cdot \nabla \boldsymbol{u} \right) = \rho \boldsymbol{g} \beta (T - T_{ref}) + \mu \nabla^2 \boldsymbol{u} - \nabla p, \tag{2.2}$$

where the term $\rho \boldsymbol{g} \beta (T - T_{ref})$ is the buoyancy estimated under the Boussinesq approximation, implying that the effect of temperature variations is considered only on liquid density ρ. Here, $\boldsymbol{g}$ is the gravity acceleration, β is the thermal expansion coefficient, and μ is the dynamic viscosity of liquid PCM. Also, $T_{ref} = (T_b + T_m)/2$ is the reference temperature, and the temperature field T is described by the energy equation

$$\frac{\partial T}{\partial t} + \frac{\mathcal{L}}{C_p} \frac{\partial f_l}{\partial t} + \boldsymbol{u} \cdot \nabla T = \alpha \nabla^2 T, \tag{2.3}$$

where the viscous dissipation is neglected as usual. Here, C_p is the specific heat capacity at constant pressure, and $\mathcal{L}$ is the melting latent heat of PCM. The second term on the left-hand side denotes the contribution from the phase change latent heat, in which $f_l = sL_y/(L_xL_y) = s/L_x$ is the melted liquid fraction, with sL_y and L_xL_y being volumes of the melted liquid layer and the cavity, respectively, as shown in figure 1. The thermo-physical properties of the solid and liquid phases are assumed to be isotropic, equal and constant. Accordingly, the velocity and thermal boundary conditions are presented as

$$\boldsymbol{u}|_{all\ walls} = 0, \tag{2.4}$$

$$T|_{left\ wall} = T_b, \quad T|_{right\ wall} = T_m \quad \text{and} \quad \left. \frac{\partial T}{\partial y} \right|_{horizontal\ walls} = 0. \tag{2.5a–c}$$

The corresponding control parameters are the Rayleigh number, the Prandtl number, the Stefan number and the aspect ratio of the cavity, which are defined respectively as

$$Ra = \frac{|\boldsymbol{g}| \beta \, \Delta T \, L_y^3}{\nu \alpha}, \quad Pr = \frac{\nu}{\alpha}, \quad Ste = \frac{C_p \, \Delta T}{\mathcal{L}} \quad \text{and} \quad \gamma = \frac{L_x}{L_y}, \tag{2.6a–d}$$

where $\Delta T = T_b - T_m$ is the temperature difference between the two vertical walls, L_x and L_y are respectively the width and height of the cavity, and $\nu = \mu/\rho$ is the kinematic viscosity of liquid PCM. The melted liquid fraction would increase monotonically during the melting process, driven by the heat flux injected from the left wall of the cavity. This flux and the resultant temperature distribution both evolve with time, and are described respectively by the averaged Nusselt number Nu and the dimensionless temperature field θ, which are defined as

$$Nu = \frac{\displaystyle\int_0^{L_y} q_x(y) \, dy}{\rho C_p \alpha \, \Delta T} \quad \text{and} \quad \theta = \frac{T - T_m}{\Delta T}, \tag{2.7a,b}$$

where $q_x(y) = u_x T - \rho C_p \alpha \, \partial T/\partial x$ is the local horizontal heat flux, with u_x being the horizontal flow velocity, and $q_x(y)$ can be simplified to $q_x(y) = -\rho C_p \alpha \, \partial T/\partial x$ at the left

wall due to the no-slip condition ($u_x = 0$) there. The above definition of *Nu* is the same as those employed in previous studies (Kakac, Aung & Viskanta 1985; Jany & Bejan 1988; Huang *et al.* 2013; Duan *et al.* 2019), and *Nu* is denoted as the ratio of the total heat transfer rate per unit length to the conductive heat transfer rate per unit length, as the corresponding dimensions of both numerator and denominator are W m^{-1}. Dividing both the numerator and the denominator by L_y, the present definition can be converted to the standard definition $Nu = -L_y^{-1} \int_0^{L_y} (\rho C_p \alpha\, \partial T/\partial x)\, \mathrm{d}y/(\rho C_p \alpha\, \Delta T/L_y)$ as in Shishkina (2016), where *Nu* is the ratio between the average horizontal heat flux and the conductive heat flux. Introducing $X = x/L_y$ and $Y = y/L_y$, the standard definition leads to another definition, $Nu = -(L_y/\Delta T) \int_0^1 (\partial T/\partial x)\, \mathrm{d}Y = - \int_0^1 (\partial \theta/\partial X)\, \mathrm{d}Y$, which is usually used for numerical calculations, indicating that *Nu* represents the dimensionless temperature gradient (Webb & Viskanta 1986; Jany & Bejan 1988; He *et al.* 2011; Rakotondrandisa, Danaila & Danaila 2019).

This system is not solvable analytically due to the mathematical difficulty; thus numerical simulations are conducted using a custom-made code by implementing the improved lattice Boltzmann method for the solid–liquid phase change developed by Huang *et al.* (2013), in order to illustrate the following analysis. The implemented numerical model has been well tested by the Stefan solution of the one-dimensional conduction melting problem, and by the 2-D convection melting problem (Huang *et al.* 2013). In this model, the immersed moving boundary scheme is adopted to simulate the evolution of the melting interface. Thus no extra velocity and thermal boundary conditions are imposed at the melting interface. In addition, the Gibbs–Thomson effect associated with the surface energy of the melting interface, which is crucial at micro-scales, is ignored herein as in the previous studies (Favier, Purseed & Duchemin 2019; Purseed *et al.* 2020; Wang *et al.* 2021*c*).

The numerical model involves the following nine parameters: the product of gravity acceleration and thermal expansion coefficient $|\boldsymbol{g}|\beta$, temperatures at the hot and cold cavity walls (T_b and T_m), numbers of grid nodes (N_x and N_y), fluid viscosity (ν), thermal diffusivity (α), the specific heat capacity at constant pressure (C_p), and the melting latent heat ($\mathcal{L}$). Amongst these parameters, the numbers of grid nodes (N_x and N_y) are selected following the rule of grid independence and the cavity aspect ratio; temperatures at the left and right walls are respectively $T_b = 400$ in lattice units and $T_m = 300$ in lattice units, and the specific heat capacity is $C_p = 1000$ in lattice units for all simulations. Then other parameters can be deduced from the Rayleigh number, the Prandtl number, the Stefan number and the Mach number $Ma = \sqrt{|\boldsymbol{g}|\beta\, \Delta T\, L_y}/C_s$, where $\sqrt{|\boldsymbol{g}|\beta\, \Delta T\, L_y}$ is the characteristic convection velocity, and $C_s = 1/\sqrt{3}$ is the sound speed in lattice units. In all simulations, *Ma* is set to 0.1 to ensure that the melted liquid flow is fully incompressible. The above parameters in the numerical simulations presented in this paper are summarised in table 2.

2.2. *Melting thermal flows*

This subsection first discusses the thermal flow without liquid–solid phase change (termed pure thermal flow) for comparison, to explore the thermal flow in the presence of a melting interface (termed melting thermal flow). Pure and melting thermal flows are both described by the conservation laws in (2.1)–(2.3), and are solved numerically by the custom-made lattice Boltzmann method code.

In the case of the pure thermal flow, the cavity is filled with liquid PCM at the start of the simulation, also presenting a uniform temperature at its melting point T_m, and the

N_x	N_y	$|g|\beta$	ν	α	$\mathcal{L}$	Dimensionless parameters
100	100	3.3×10^{-7}	0.0052	0.2582	1.0×10^7	$Ra = 2.5 \times 10^4, Pr = 0.02$
						$Ste = 0.01, \gamma = 1.0$
						$Ma = 0.1$ (figures 2–4)
1500	1000	3.3×10^{-8}	0.0141	0.2357	1.7×10^6	$Ra = 1.0 \times 10^6, Pr = 0.06$
						$Ste = 0.06, \gamma = 1.5$
						$Ma = 0.1$ (figure 4)
400	400	8.3×10^{-8}	0.0103	0.5164	5.0×10^5	$Ra = 1.0 \times 10^5, Pr = 0.02$
						3.3×10^5
						2.5×10^5

					$\mathcal{L}$	Dimensionless parameters
					5.0×10^5	$Ra = 1.0 \times 10^5, Pr = 0.02$
					3.3×10^5	$\gamma = 1.0, Ma = 0.1$ (figure 6)
					2.5×10^5	$Ste = 0.2, 0.3, 0.4$

Table 2. Numerical parameters in the simulations presented in the figures.

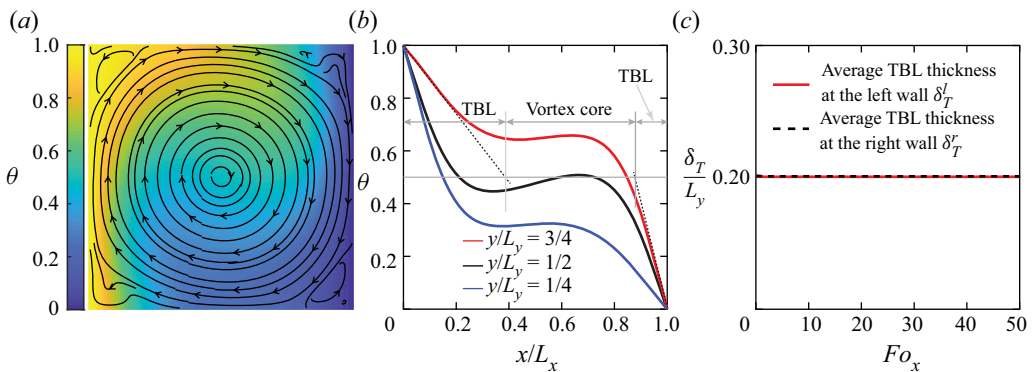Figure 2. Steady pure thermal flow at $Ra = 2.5 \times 10^4$, $Pr = 0.02$, $Ste = 0.01$ and $\gamma = 1$. (*a*) Dimensionless temperature field θ and streamlines. (*b*) Local temperature profiles at three altitudes. (*c*) Average thicknesses of TBLs at the left and right walls.

boundary conditions are exactly the same as shown in figure 1. The left wall temperature is raised at some point, and the liquid PCM will start to flow under the temperature difference ΔT between the two vertical walls, reaching a steady state after a sufficiently long time. A series of numerical simulations is conducted, and similar flow patterns are observed. The resultant velocity and temperature fields of one typical case are shown in figure 2(*a*). This figure reveals that, in addition to the large convective vortex, whose size is comparable to the size of the cavity, four small convective corner rolls also exist due to the confinement of cavity walls, where the flow velocity is low. Moreover, the convective roll at the bottom right corner presents the lowest temperature. Analogically speaking, in the case of melting thermal flow, the solid PCM at the bottom right corner, wherein the thermal convection is also the weakest, will be the most difficult part to be melted.

The local temperature profiles at three altitudes, $y = L_y/4$, $L_y/2$ and $3L_y/4$, are shown in figure 2(*b*), and a sandwich structure is observed. Two thermal boundary layers (TBLs) are present at the left and right walls, and their local thicknesses are not equal at the same altitude y, except at $y = L_y/2$. This is due to the local heat accumulation along the flow directions near the vertical walls, as shown in figure 2(*a*). The local temperature profile in the x-direction is linear within the TBL, and presents nearly a plateau in between, corresponding to the vortex core. The temperature variation is limited within the two TBLs. Thus the average TBL thickness δ_T can be estimated by extrapolating the

950 A34-8

temperature profile linearly to $\Delta T/2$, i.e. $\theta = 0.5$:

$$\delta_T = -(\Delta T/2)/(\partial \bar{T}/\partial x), \tag{2.8}$$

where $\bar{T} = \int_0^{L_y} T \, dy/L_y$ is the average temperature over the vertical wall, or the melting interface in the case of melting thermal flows (Belmonte, Tilgner & Libchaber 1994; Takeshita *et al.* 1996; Verzicco & Camussi 1999; Zhou *et al.* 2010; Zhou & Xia 2010; Scheel & Schumacher 2014; Ng *et al.* 2015). Then the total heat transfer rate per unit length injected from the left wall is evaluated as $\int_0^{L_y} q_x \, dy = -\rho C_p \alpha \, (\partial \bar{T}/\partial x) \, L_y = \rho C_p \alpha \, \Delta T \, L_y/(2\delta_T)$, which is indeed independent of the cavity height L_y due to the fact that L_y/δ_T is invariant once the Rayleigh number and Prandtl number are given (Shishkina 2016). Introducing the definition of Nu in (2.7*a,b*), the average Nusselt number is obtained as

$$Nu = L_y/(2\delta_T). \tag{2.9}$$

As expected, the average thicknesses of the TBLs at the left and right walls are the same (figure 2*c*), because the energy conservation at the steady state requires that the input energy from the left wall, characterised by $Nu^l = L_y/(2\delta_T^l)$, should be equal to the output energy from the right wall, characterised by $Nu^r = L_y/(2\delta_T^r)$, where δ_T^l and δ_T^r are the average TBL thicknesses at the left and right walls of the cavity, respectively.

Furthermore, the average Nusselt number can be related to the dimensionless control parameters. For a laminar pure thermal flow, the scaling law for Nu has been derived theoretically as $Nu \sim Ra^{1/4} Pr^{1/4}$ for $Pr \leq 0.1$, and $Nu \sim Ra^{1/4} Pr^0$ for $Pr > 0.1$, and validated in the range $10^5 \leq Ra \leq 10^{10}$ (Shishkina 2016). Later, Q. Wang *et al.* (2021) confirmed this scaling law numerically, providing a scaling law $Nu \sim Ra^{0.26}$ for $Pr > 0.1$. Combining these results, the average Nusselt number is fitted and expressed as

$$Nu = \begin{cases} 0.53 \, Ra^{1/4} \, Pr^{1/4}, & \text{if } Pr \leq 0.1, \\ 0.24 \, Ra^{0.26} \, Pr^0, & \text{elsewhere.} \end{cases} \tag{2.10}$$

It is worth noticing that the theoretically predicted scaling $Nu \sim Ra^{1/4}$ at $Pr > 0.1$ also fits the data reported by Shishkina (2016) and Q. Wang *et al.* (2021), and presents a negligible difference from $Nu \sim Ra^{0.26}$ at high Ra. However, at low Ra, $Nu \sim Ra^{1/4}$ shows a noticeable deviation with respect to the previous data, as observed by Q. Wang *et al.* (2021). Thus we choose to employ $Nu \sim Ra^{0.26}$ at $Pr > 0.1$, as in (2.10).

According to (2.9), the average TBL thickness normalised by L_y is then

$$\frac{\delta_T}{L_y} = \begin{cases} 0.94 \, Ra^{-1/4} \, Pr^{-1/4}, & \text{if } Pr \leq 0.1, \\ 2.08 \, Ra^{-0.26} \, Pr^0, & \text{elsewhere,} \end{cases} \tag{2.11}$$

predicting $\delta_T/L_y = 0.1988$ for $Ra = 2.5 \times 10^4$ and $Pr = 0.02$, which is in good agreement with the numerical result (figure 2*c*).

For the melting thermal flow, simulations are conducted under the same boundary conditions as those for the pure thermal flow, except that the cavity is initially filled with solid PCM, and an evolving melting interface exists. In the simulations, the melting interface is located by connecting the mesh points with a local melting fraction $1/2$, and will overlap with the right cold wall at the end of the melting process.

The interface evolution behaviours and corresponding thermal flow dynamics are similar in different simulations. To illustrate the melting process, the time evolution of the melting interface for a typical case, with the accompanying flow and temperature fields appended, is shown in figures 3(*a–c*). These melting processes are usually interpreted by

the well-known two-stage melting model (Bareiss & Beer 1984; Ho & Viskanta 1984; Gau & Viskanta 1986; Wolff & Viskanta 1988; Bertrand *et al.* 1999; Wang *et al.* 1999; Du *et al.* 2007; Huang *et al.* 2013; Shokouhmand & Kamkari 2013; Li *et al.* 2014; Luo *et al.* 2015; Hamad *et al.* 2017, 2021). In the first stage, the melted liquid layer is thin; thus the viscosity dominates the flow. Accordingly, the heat is transferred via conduction; therefore the melting interface remains parallel with the left wall (figure 3*a*). As time goes by, the melted liquid layer thickens increasingly, and the buoyancy gradually overcomes the viscosity to dominate the flow. Consequently, the rising hot liquid continuously scours the upper region of the PCM, and generates a distorted melting interface (figure 3*b*). In this second stage, thermal convection comes into play and eventually dominates the heat transfer. In addition, a part of the right cold wall will be exposed directly to the hot melted liquid during the final phase of the melting process (figure 3*c*), as observed in the existing studies (Bénard *et al.* 1985; Duan *et al.* 2019; Rakotondrandisa *et al.* 2019; Yang *et al.* 2019). In these studies, this final phase of the melting process is considered to be the last part of the second convection stage. However, their f_l versus Fo_x curves reveal that the melting rate $\partial f_l / \partial Fo_x = \partial (s/L_x)/\partial Fo_x$ will decrease significantly as in figure 3(*e*) once the cold cavity wall is exposed to the melted liquid, indicating the change in heat transfer characteristics. Thus introducing a third stage is necessary to characterise the melting process. Meanwhile, in the bottom right corner where the remnant solid PCM is left, the thermal convection will decay significantly as informed by the discussions on the pure thermal flow. Thus this third stage is referred to as 'the decaying convection stage'. Consequently, the traditional two-stage model should be updated to a three-stage melting model, including conduction, convection and decaying convection.

For the thermal convection, it is found that the convection intensity gathers mainly at the upper part of the cavity due to the buoyancy in the second and third stages, and becomes negligible close to the bottom wall (figures 3*b*,*c*). That is, the propagation of the horizontal intersection x_0 between solid PCM and the cavity bottom wall is driven by conduction, indicating $x_0/L_x \sim \sqrt{Fo_x}$ as stated by Hamdan & Elwerr (1996) and Hamdan & Al-Hinti (2004). To have a convincing validation, x_0 from the presented simulation in figures 3(*a*–*c*) and those reported in the studies of Rakotondrandisa *et al.* (2019) and Bénard *et al.* (1985), are normalised by L_x and presented as functions of Fo_x as shown in figure 3(*d*). Accordingly, the fitting correlations of the three data sets are $x_0/L_x = 0.13 \, Fo_x^{0.50}$, $x_0/L_x = 0.25 \, Fo_x^{0.52}$ and $x_0/L_x = 0.52 \, Fo_x^{0.53}$, where the scaling exponents are very close to the expected value of $1/2$, and increase very slightly when Ra varies widely from 10^4 to 10^9. This finding indicates that the conduction dominance at the bottom wall is reasonable.

The following discusses the TBLs in the melting thermal flow. In figure 3(*e*), the average thickness of the TBL at the left wall (δ_T^l) and that at the melting interface (δ_T^i) are shown for the melting case presented in figures 3(*a*–*c*). Meanwhile, the average thicknesses of the melted liquid layer (*s*) from the present simulation and those from Huang *et al.* (2013) are also appended for comparison, wherein a good agreement is achieved. For the configuration under consideration, the first stage lasts for $Fo_x \leq 2.7$ (figure 3*e*), where the melted liquid layer is saturated with TBLs, i.e. $s = \delta_T^l + \delta_T^i$, verifying the dominance of conduction in the heat transfer mechanism. In the second stage ($2.7 < Fo_x \leq 25.9$), thermal convection is sufficiently strong to separate the two TBLs; thus $s > \delta_T^l + \delta_T^i$, constituting a sandwich structure as well. In the third stage ($Fo_x > 25.9$), $s > \delta_T^l + \delta_T^i$ still holds, while δ_T^i in this stage comprises two parts: TBLs along the liquid–solid PCM interface and the uncovered right cold wall (figure 3*c*). As for the relation between δ_T^l and δ_T^i, it is found that they are approximately equal to each other, rather than the identical
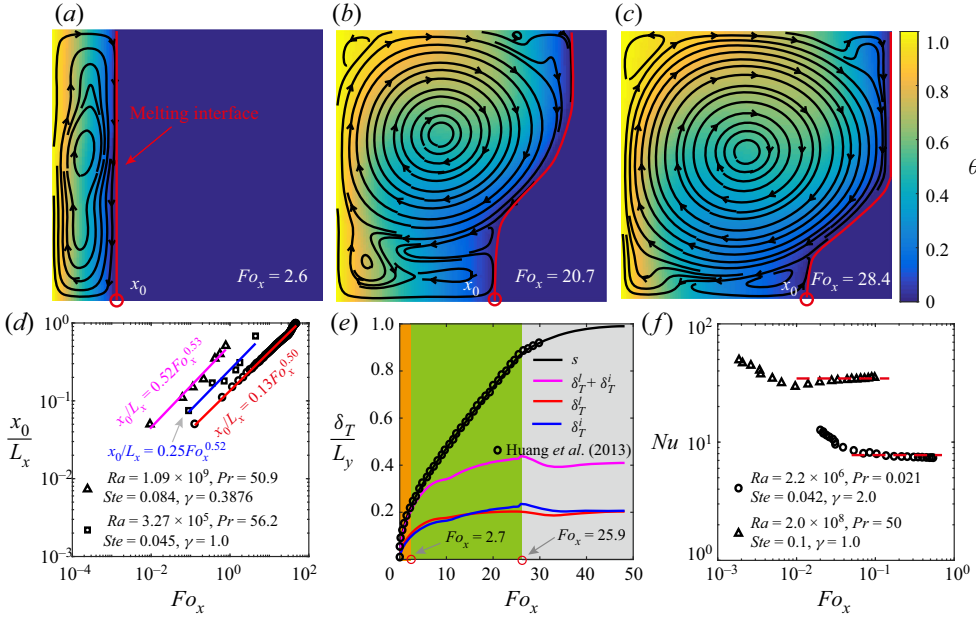
Figure 3. Melting thermal flow at $Ra = 2.5 \times 10^4$, $Pr = 0.02$, $Ste = 0.01$ and $\gamma = 1$. (*a–c*) Dimensionless temperature fields and streamlines. (*d*) Horizontal intersection between solid PCM and the bottom wall (x_0) from present simulation (circles), from Rakotondrandisa *et al.* (2019) (squares), and from Bénard *et al.* (1985) (triangles). (*e*) Comparison between average thicknesses of TBLs (δ_T^l and δ_T^i) and the average thickness of the melted liquid layer (*s*). Three melting stages are in turn labelled in orange, green and grey in the background. (*f*) The average Nusselt number *Nu* obtained from the melting thermal flows performed by Webb & Viskanta (1986) (circles) and Rakotondrandisa *et al.* (2019) (triangles). The red dashed line is *Nu* scaling (see (2.10)) developed in the pure thermal flow by Shishkina (2016).

equality as observed in the pure thermal flow (figure 2*c*). Such an approximately equal behaviour can also be explained from the viewpoint of energy conservation. PCM melting is an unsteady process, wherein the bulk temperature of the melted liquid varies over time. Consequently, the input energy, characterised by $Nu^l = L_y/(2\delta_T^l)$, is divided into two parts: one is responsible for the variation of the bulk temperature of the melted liquid, corresponding to the sensible heat; the other is transferred to the melting interface, characterised by $Nu^i = L_y/(2\delta_T^i)$, to compensate for the melting latent heat or the leaking energy through the uncovered right cold wall. The sensible heat is negligible due to the low Stefan number under consideration, resulting in $Nu^l \approx Nu^i$; thus $\delta_T^l \approx \delta_T^i$. The approximately equal $Nu^l \approx Nu^i$ has also been reported by Bénard *et al.* (1985), wherein $Ste = 0.084$.

Furthermore, it is easy to conclude that the average thickness of the TBL is $\delta_T^l = \delta_T^i = s/2$ in the conduction-dominated first stage, after which a comparison between figures 2(*c*) and 3(*e*) shows that the average TBL thicknesses in the melting thermal flow are approximate to those in the corresponding pure thermal flow. In addition to the data in the present study, the results from the existing studies are also presented in figure 3(*f*). The averaged Nusselt number in the melting thermal flows reported by Webb & Viskanta (1986) and Rakotondrandisa *et al.* (2019) are approximately equal to their counterparts in pure thermal flows, as discussed by Shishkina (2016). Considering $Nu = L_y/(2\delta_T)$, the averaged TBL thicknesses in a melting thermal flow are approximately equal to those in the pure thermal flow under the same configurations. Herein, the approximate equality

950 A34-11

is attributed to the energetically expensive PCM melting at low *Ste*; thus a time scale separation between the thermal convection and the melting interface migration exists. That is, thermal convection at low *Ste* would adapt rapidly to the melting interface migration, being in a nearly quasi-steady state. Thus approximately equal average TBL thicknesses are observed in melting and pure thermal flows under the same configurations. This approximate equality has also been observed in pure and melting Rayleigh–Bénard convections (Esfahani *et al.* 2018).

   In summary, a comparison with the pure thermal flow deepens the understanding of the melting thermal flow, and the following conclusive points, which will inform the theoretical modelling in the subsequent section, are realised. (I) In addition to the conduction–convection two-stage description, a third melting stage is suggested, wherein the melting rate decreases continuously until the end of the melting process. (II) The propagation of the horizontal intersection x_0 between solid PCM and the cavity bottom wall is driven by heat conduction. (III) The average thickness of the TBL at the left wall (δ_T^l) and that at the melting interface (δ_T^i) are approximately equal at low *Ste*. (IV) In the first stage, the average thickness of the TBL is $\delta_T = s/2$, and after this stage, the averaged TBL thickness in the melting thermal flow is approximately equal to that in the pure thermal flow under the same configurations.

3. Predictions

Theoretical analyses on the melting problem presented in § 2.1 are performed in this section, based on the discussions in § 2.2.

   The vicinity region within the TBL is examined to describe the evolution of the melting interface. The vertically averaged position of the melting interface (dashed line in figure 1) is denoted by *s*. The velocity $\boldsymbol{u}$ is negligible when the melted liquid flow is close to the interface, due to the no-slip condition therein. Accordingly, (2.3) in the limit of $x \to s$ simplifies to

$$\frac{\partial T}{\partial t} + \frac{\mathcal{L}}{C_p} \frac{\partial f_l}{\partial t} = \alpha \nabla^2 T. \tag{3.1}$$

In addition to θ, the following dimensionless quantities are further introduced:

$$x' = x/\delta_T, \quad y' = y/L_y \quad \text{and} \quad t' = t/t_0, \tag{3.2a-c}$$

where t_0 is the characteristic time necessary to achieve a melted liquid fraction of f_l. Equation (3.1) is then normalised as follows:

$$\frac{\partial \theta}{\partial t'} + \frac{1}{Ste} \frac{\partial f_l}{\partial t'} = \frac{\alpha t_0}{\delta_T^2} \left(\frac{\partial^2 \theta}{\partial x'^2} + \frac{\delta_T^2}{L_y^2} \frac{\partial^2 \theta}{\partial y'^2} \right). \tag{3.3}$$

On the one hand, thermal energy for a PCM is stored mainly in the form of latent heat rather than sensible heat. It thus leads to $1/Ste \gg 1$, indicating that the first unsteady term on the left-hand side is negligible compared with the second one. On the other hand, the average thickness δ_T of the TBL is usually substantially smaller than the cavity length scale L_y. Thus only the temperature gradient along the *x*-direction is retained in the

950 A34-12

diffusive term. Therefore, (3.3) is further simplified to

$$\frac{1}{Ste}\frac{\partial f_l}{\partial t'} = \frac{\alpha t_0}{\delta_T^2}\frac{\partial^2 \theta}{\partial x'^2}, \tag{3.4}$$

and its dimensional form is

$$\mathcal{L}\frac{\partial f_l}{\partial t} = C_p \alpha \frac{\partial^2 T}{\partial x^2}. \tag{3.5}$$

That is, the latent heat necessary for the PCM melting is compensated by the thermal diffusion in the *x*-direction. Integrating the above equation over the cavity ($0 \leq x \leq L_x$, $0 \leq y \leq L_y$) as in the previous studies (Esfahani *et al.* 2018; Favier *et al.* 2019), the following can be obtained:

$$\mathcal{L}\frac{\partial f_l}{\partial t}L_x L_y = C_p \alpha \int_0^{L_y}\left[\left(\frac{\partial T}{\partial x}\right)_r - \left(\frac{\partial T}{\partial x}\right)_l\right]\mathrm{d}y, \tag{3.6}$$

where the subscripts '*r*' and '*l*' denote the right ($x = L_x$) and left ($x = 0$) walls, respectively, $-C_p \alpha \int_0^{L_y}(\partial T/\partial x)_l\,\mathrm{d}y > 0$ is the input energy, and $C_p \alpha \int_0^{L_y}(\partial T/\partial x)_r\,\mathrm{d}y \leq 0$ is the leaking energy through the right cold wall.

3.1. *Predictions for the first and second stages*

Three stages are identified for the PCM melting in a rectangle cavity. This subsection considers the first and second stages, where the right wall of the cavity is covered entirely by the solid PCM with the same temperature T_m; thus no energy leaks out. This leads from (3.6) to

$$\mathcal{L}\frac{\partial f_l}{\partial t}L_x L_y = -C_p \alpha \left(\frac{\partial \bar{T}}{\partial x}\right)_l L_y. \tag{3.7}$$

Considering $f_l = s/L_x$, this equation becomes

$$\frac{\partial s}{\partial t} = -\frac{C_p \alpha}{\mathcal{L}}\left(\frac{\partial \bar{T}}{\partial x}\right)_l = \frac{C_p \alpha}{\mathcal{L}}\frac{\Delta T}{2\delta_T}, \tag{3.8}$$

where (2.8) is used to relate δ_T and the average temperature gradient. It should be noted that (3.8) is applicable for only the first and second stages. In the third stage, a part of the right cold wall is directly exposed to the melted liquid (figure 3*c*), thus inducing energy leakage. Then (3.6) becomes $\mathcal{L}(\partial f_l/\partial t)L_x L_y < -C_p \alpha(\partial \bar{T}/\partial x)_l L_y$, explaining the melting rate in the third stage being smaller than that (see (3.7)) in the second stage, as observed in figure 3(*e*) and existing studies (Bénard *et al.* 1985; Duan *et al.* 2019; Rakotondrandisa *et al.* 2019; Yang *et al.* 2019).

Section 2.2 concluded that after the first stage, the average thickness of the TBL in a melting thermal flow is approximately equal to that (see (2.11)) in the pure thermal flow under the same configuration. Meanwhile, $\delta_T = s/2$ in the first stage; thus the average TBL thickness in melting thermal flows can be summarised as

$$\delta_T = \min(s/2, kL_y Ra^m Pr^n), \tag{3.9}$$

where $k = 0.94$, $m = -0.25$, $n = -0.25$ for $Pr \leq 0.1$, and $k = 2.08$, $m = -0.26$, $n = 0$ for $Pr > 0.1$, as indicated in (2.11).

Substituting (3.9) into (3.8), the average thickness of the melted liquid layer s is then obtained by integration as

$$
s = \begin{cases} \sqrt{2\alpha t\, Ste}, & \text{if } s \leq 2kL_y\, Ra^m\, Pr^n, \\ \dfrac{\alpha t\, Ste}{2kL_y\, Ra^m\, Pr^n} + kL_y\, Ra^m\, Pr^n, & \text{elsewhere,} \end{cases} \tag{3.10}
$$

where we have imposed the boundary conditions that $s(t=0) = 0$ and s is a continuous function with respect to t. Consequently, the melted liquid fraction f_l during the first and second stages is derived macroscopically as

$$
f_l = \frac{s}{L_x} = \begin{cases} \sqrt{2\, Fo_x\, Ste}, & \text{if } f_l \leq 2k\, Ra^m\, Pr^n/\gamma, \\ \gamma\, Fo_x\, Ste/(2k\, Ra^m\, Pr^n) + k\, Ra^m\, Pr^n/\gamma, & \text{elsewhere,} \end{cases} \tag{3.11}
$$

where $s/L_y = \gamma s/L_x = \gamma f_l$ were used.

3.2. *Prediction for the third stage*

In the third stage, the upper part of the cavity right cold wall is exposed to the hot liquid PCM, and the remnant solid PCM is located in the bottom right corner, which is simplified into a rectangle with $x_0 \leq x \leq L_x$ and $0 \leq y \leq y_0$, as shown in figure 4(*a*). In this stage, the energy reaching the melting interface is divided into two parts (figure 4*a*): the part at $0 \leq y \leq y_0$ drives the PCM melting, and the other part at $y_0 \leq y \leq L_y$ leaks out through the uncovered right cold wall. Thus the leaking energy can be estimated as $C_p\alpha\, (\partial\bar{T}/\partial x)_i\, (L_y - y_0)$, with the subscript '$i$' denoting the melting interface. Substituting this estimation into (3.6), one gets

$$
\mathcal{L}\frac{\partial f_l}{\partial t}\, L_x L_y = C_p\alpha\left(\frac{\partial\bar{T}}{\partial x}\right)_i (L_y - y_0) - C_p\alpha\left(\frac{\partial\bar{T}}{\partial x}\right)_l L_y = -C_p\alpha\left(\frac{\partial\bar{T}}{\partial x}\right)_l y_0, \tag{3.12}
$$

where the equation on the right is obtained from that at low Ste, $\delta_T^l \approx \delta_T^i$; thus $(\partial\bar{T}/\partial x)_l \approx (\partial\bar{T}/\partial x)_i$, as discussed in § 2.2.

Equations (3.7) and (3.12) indicate that the melting rate ($\partial f_l/\partial t$) depends only on the averaged input heat flux $-C_p\alpha\, (\partial\bar{T}/\partial x)_l = C_p\alpha\, \Delta T/(2\delta_T)$, and the vertical projected areas of the solid PCM, which are L_y and y_0 in the first two stages and the third one, respectively. This is consistent with the result of Baehr & Stephan (2011), who showed that the thermal power, proportional to the melting rate in the present study, is determined by the dot product between the average input heat flux ($\boldsymbol{q}$) and the surface element ($\boldsymbol{A}$) as $\boldsymbol{q} \cdot \boldsymbol{A} = |\boldsymbol{q}|\, |\boldsymbol{A}|\cos\psi$, thus depending on the projected area $|\boldsymbol{A}|\cos\psi$ rather than the absolute area $|\boldsymbol{A}|$. Here, ψ is the local intersection angle between $\boldsymbol{q}$ and $\boldsymbol{A}$.

In addition, δ_T in the second and third stages is approximately the same (figures 3*e*,*f*), because in these two stages the thermal convection takes effect and the characteristic convection velocity ($\sqrt{|\boldsymbol{g}|\beta\, \Delta T\, L_y}$) is invariant, resulting in an unchanged average TBL thickness δ_T. Thus (3.12) can be divided by (3.7) to cancel out the average temperature gradient, resulting in

$$
\left(\frac{\partial f_l}{\partial t}\right)_3 \Big/ \left(\frac{\partial f_l}{\partial t}\right)_2 = \frac{y_0}{L_y}, \tag{3.13}
$$

where subscripts '2' and '3' denote the second and third stages, respectively. This equation indicates clearly that the melting rate in the third stage will gradually decrease compared with that in the second one, because y_0 will gradually move downwards as the melting
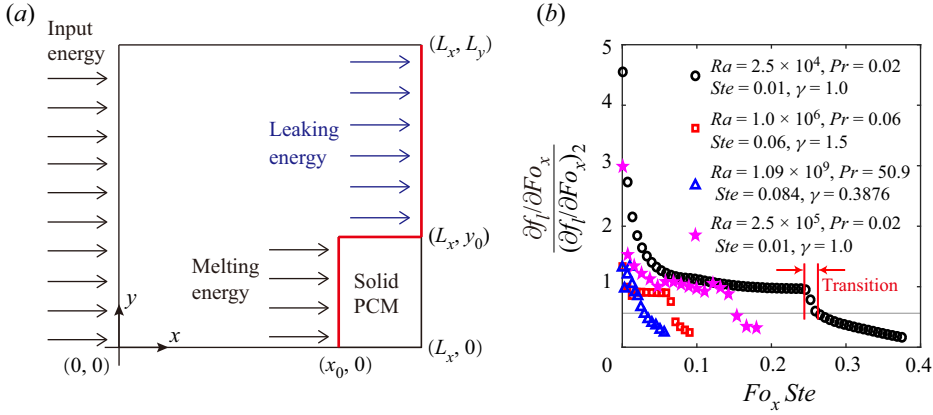
950 A34-14

Figure 4. (*a*) Schematic of the PCM melting during the third stage, where the red line is the melting interface, and its upper part ($y_0 \leq y \leq L_y$) overlaps the uncovered right cold wall. (*b*) Melting rate of three stages normalised by that of the second stage. In addition to the present simulations (circles and squares), the results from Bénard *et al.* (1985) (triangles) and Huang *et al.* (2013) (stars) are also presented.

continues. Therefore, this equation attributes the continuously decreasing melting rate in the third stage to the decrease in the vertical projected area, which, relatively speaking, is more direct in understanding than the explanation by Shokouhmand & Kamkari (2013). They explained that the decreasing melting rate is attributed to the depression of the convection current, due to the increase in the bulk temperature of liquid PCM and the stratification of temperature fields.

Close to the bottom wall, heat transfer is dominated by conduction (Hamdan & Elwerr 1996), as discussed in § 2.2. Introducing the values of *Ste* in figure 3(*d*) into the first branch of (3.10), the horizontal intersections are calculated as $x_0/L_x = s/L_x = 0.14\sqrt{Fo_x}$, $x_0/L_x = s/L_x = 0.30\sqrt{Fo_x}$ and $x_0/L_x = s/L_x = 0.41\sqrt{Fo_x}$, where the multiplicative factors (0.14, 0.30 and 0.41) are respectively close to the fitting coefficients 0.13, 0.25 and 0.52 in figure 3(*d*). Thus the horizontal intersection $x_0 = s$ can be calculated from the present conduction solution, yielding

$$x_0 = L_x\sqrt{2Fo_x\,Ste}. \tag{3.14}$$

The vertical intersection y_0 between solid PCM and the right wall (figure 4*a*) is estimated from the definition of melted liquid fraction $f_l = 1 - (L_x - x_0)y_0/(L_xL_y)$ as

$$\frac{y_0}{L_y} = \frac{1 - f_l}{1 - \sqrt{2Fo_x\,Ste}}. \tag{3.15}$$

During the second stage, the melting rate $\partial f_l/\partial Fo_x$ is obtained from the second branch of (3.11) as

$$\left(\frac{\partial f_l}{\partial Fo_x}\right)_2 = \frac{\gamma\,Ste}{2k\,Ra^m\,Pr^n}, \tag{3.16}$$

which is obviously a constant over time. Then, according to (3.13), the melting rate in the third stage is evaluated as

$$\left(\frac{\partial f_l}{\partial Fo_x}\right)_3 = \frac{y_0}{L_y}\frac{\gamma\,Ste}{2k\,Ra^m\,Pr^n} = \frac{1 - f_l}{1 - \sqrt{2Fo_x\,Ste}}\frac{\gamma\,Ste}{2k\,Ra^m\,Pr^n}, \tag{3.17}$$

950 A34-15

where (3.15) and (3.16) were introduced. Assuming that the third stage starts from the point (Fo_x^c, f_l^c), an integration of (3.17) then gives

$$f_l = 1 - (1 - f_l^c) \left(\frac{1 - \sqrt{2Fo_x\,Ste}}{1 - \sqrt{2Fo_x^c\,Ste}} \right)^{\gamma/(2k\,Ra^m\,Pr^n)} \exp\left[\frac{\gamma\,(\sqrt{2Fo_x\,Ste} - \sqrt{2Fo_x^c\,Ste})}{2k\,Ra^m\,Pr^n} \right]. \tag{3.18}$$

In order to predict f_l^c, the melting rate of the entire melting process is divided by that of the second stage as $(\partial f_l/\partial Fo_x)/(\partial f_l/\partial Fo_x)_2$, as shown in figure 4(*b*). In this figure, a very short transition from the second to the third stages is observed, where the ratio sharply decreases from 1 to around 0.5. As denoted by (3.13), this ratio after the second stage is equal to y_0/L_y. Therefore, the sharp decrease indicates that the vertical intersection between solid PCM and the right wall moves downwards rapidly when $y_0/L_y > 0.5$. This is quite reasonable because the thermal convection intensity concentrates mainly on the upper part of the cavity due to buoyancy. Meanwhile, the transition is very short-lived; therefore it is reasonable to assume that the starting point of the third stage is also the end point of the second stage. Thus the transition point (Fo_x^c, f_l^c) satisfies the equations

$$\left(\frac{y_0}{L_y} \right)_c = \frac{1 - f_l^c}{1 - \sqrt{2Fo_x^c\,Ste}} \approx \frac{1}{2}, \tag{3.19}$$

$$f_l^c = \gamma\,Fo_x^c\,Ste/(2k\,Ra^m\,Pr^n) + k\,Ra^m\,Pr^n/\gamma, \tag{3.20}$$

where the second equation is the second branch of (3.11). Combining the two equations above, the following is obtained:

$$\left. \begin{array}{l} f_l^c = \frac{1}{2} + \sqrt{\mathcal{A} + \mathcal{B}}, \\ \mathcal{A} = \frac{1}{2}k\,Ra^m\,Pr^n\,(\gamma - k\,Ra^m\,Pr^n)/\gamma^2, \\ \mathcal{B} = \frac{1}{2}k\sqrt{2\gamma k\,Ra^{3m}\,Pr^{3n} - 3k^2\,Ra^{4m}\,Pr^{4n}}/\gamma^2 \end{array} \right\} \tag{3.21}$$

and

$$Fo_x^c = 2k\,Ra^m\,Pr^n\,(f_l^c - k\,Ra^m\,Pr^n/\gamma)/(\gamma\,Ste). \tag{3.22}$$

The onset of the third stage, (f_l^c, Fo_x^c), has now been determined. Further combining (3.11) and (3.18), the full prediction for the melted liquid fraction at all stages is obtained as

$$f_l = \begin{cases} \sqrt{2Fo_x\,Ste}, & \text{if } f_l \leq 2k\,Ra^m\,Pr^n/\gamma, \\ \gamma\,Fo_x\,Ste/(2k\,Ra^m\,Pr^n) + k\,Ra^m\,Pr^n/\gamma, & \text{if } 2k\,Ra^m\,Pr^n/\gamma \leq f_l \leq f_l^c, \\ 1 - (1 - f_l^c) \left(\dfrac{1 - \sqrt{2Fo_x\,Ste}}{1 - \sqrt{2Fo_x^c\,Ste}} \right)^{\gamma/(2k\,Ra^m\,Pr^n)} \\ \quad \times \exp\left[\dfrac{\gamma\,(\sqrt{2Fo_x\,Ste} - \sqrt{2Fo_x^c\,Ste})}{2k\,Ra^m\,Pr^n} \right], & \text{elsewhere.} \end{cases} \tag{3.23}$$

This prediction contains the effects of all dimensionless control numbers under consideration, and is valid when *Ste* is sufficiently small. The upper limit of *Ste* will be discussed in the next subsection.

950 A34-16

3.3. *Validation*

In this subsection, the predicted melted liquid fraction f_l (see (3.23)) is validated by comparing with the reported data, which are mainly from the previous studies listed in table 1. Note that the numerical data obtained by Jany & Bejan (1988) cited in table 1 are not employed herein, because their correlation (and thus the numerical data) greatly overestimates the existing experiment and numerical results, as indicated by Duan *et al.* (2019). Moreover, the experimental studies by Wolff & Viskanta (1988), Wang *et al.* (1999) and Du *et al.* (2007) used multiple group data to fit their f_l correlations. However, the authors did not provide complete information regarding dimensionless control parameters; thus their data are not employed herein either. In order to perform a thorough validation, the numerical results from Huang *et al.* (2013) and Rakotondrandisa *et al.* (2019) are also supplemented.

The collected reported data cover a wide range of dimensionless control parameters (Ho & Viskanta 1984; Bénard *et al.* 1985; Gau & Viskanta 1986; Brent *et al.* 1988; Chakraborty & Chatterjee 2007; Huang *et al.* 2013; Duan *et al.* 2019; Faden *et al.* 2019; Rakotondrandisa *et al.* 2019), namely $2.5 \times 10^5 \leq Ra \leq 1.09 \times 10^9$, $0.02 \leq Pr \leq 56.2$, $0.01 \leq Ste \leq 0.132$ and $0.3876 \leq \gamma \leq 1.4$. Figure 5 shows that although the reported data resulted in a series of different fitting correlations as summarised in table 1, all these data can be predicted by the present solution (see (3.23)). By contrast, the prediction accuracy in the third stage is less satisfying than that in the first and second stages (figures 5d–f). This is probably due to the rectangular simplification of remnant solid PCM (figure 4a), and the approximation in the derivation of f_l^c (see (3.19)). Nevertheless, in the present validation, the maximum relative error $E_r = \{|f_l^p - f_l^t|/f_l^t\}_{max}$ in the third stage is still within 10 %, where the superscripts 'p' and 't' represent the prediction and reported results, respectively.

The previous section indicated that the prediction (3.23) is valid only at low Stefan numbers. We discuss now its upper limit in a numerical way due to the lack of reported experimental measurements. In figure 6, the predicted f_l is compared to the simulated data. As expected, the relative error between the present solution and the simulation result rises as Ste increases. It is found that Ste should not exceed 0.3, when the maximum relative error E_r is required to be less than 10 %.

4. Discussions

This section will first explain further the effect of the distorted melting interface. Parameter space and 3-D effect will then be discussed, and transitions between the two successive stages will be discussed as well in the end.

4.1. *Effect of the distorted melting interface*

During the melting process, the geometry of the melted liquid layer, characterised by the melting interface, is evolving continuously, and its influence on melted liquid flow and heat transfer is incorporated in the derivation implicitly, by the average input heat flux $(C_p \alpha \Delta T/(2\delta_T))$ and the vertical projected area of the solid PCM. The two factors determine the melting rate uniquely, as mentioned previously.

In the first and second stages, the solid PCM occupies the entire right cold wall, and the vertical projected area is always L_y, regardless of whether the melting interface is distorted or not. Thus the influence of altered geometry is exerted on the melting rate by changing the average input heat flux, which is incorporated in the model via the average
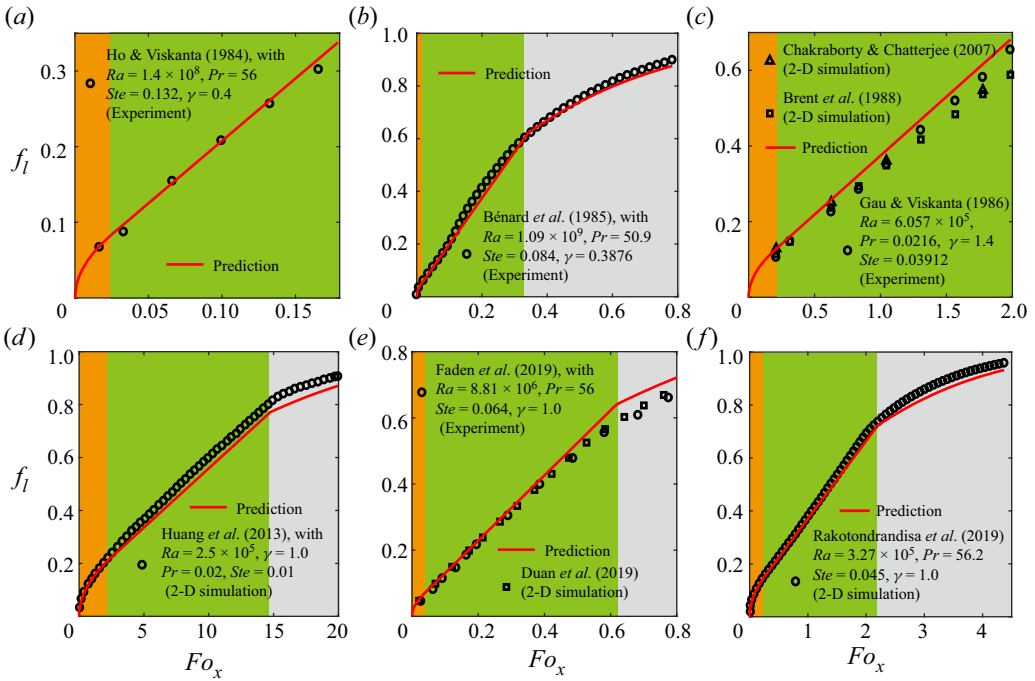
Figure 5. The predictions are tested against the reported data available with different PCMs: (*a*) and (*b*) *n*-octadecane; (*c*) gallium; (*d*) tin; (*e*) and (*f*) *n*-octadecane. In all panels, the orange, green and grey backgrounds are used to denote the first (conduction), the second (convection) and the third (decaying convection) stages, respectively.
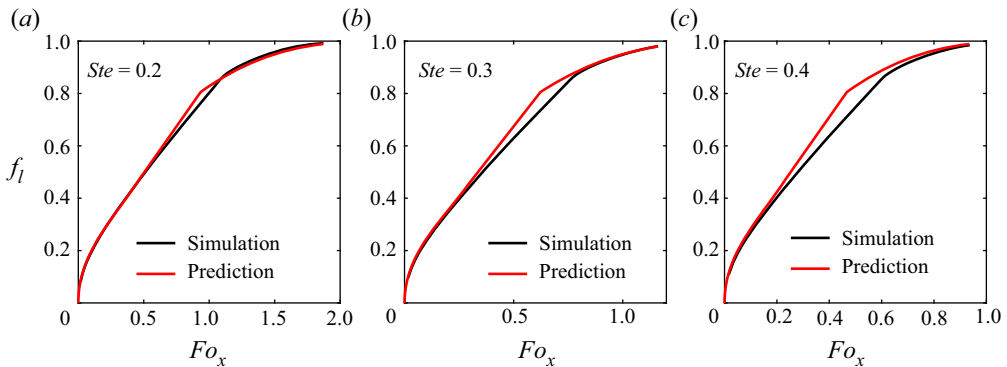

Figure 6. The upper limit of *Ste*. Simulations and predictions are performed with $Ra = 1.0 \times 10^5$, $Pr = 0.02$ and $\gamma = 1.0$: (*a*) $Ste = 0.2$, (*b*) $Ste = 0.3$, and (*c*) $Ste = 0.4$.

thickness of the TBL, $\delta_T = \min(s/2, kL_y Ra^m Pr^n)$ (see (3.9)). This expression indicates that in the first stage, the heat conduction will increase the aspect ratio of the melted liquid geometry (s/L_y), and thus thicken the TBL. In the second stage, the altered geometry will not change the average thickness of the TBL, because during this stage, thermal convection takes effect and the characteristic convection velocity ($\sqrt{|\boldsymbol{g}|\beta\,\Delta T\,L_y}$) is irrelevant to s, resulting in the fact that δ_T is also independent of s. In the third stage, the average input

950 A34-18

heat flux also remains unchanged, for the same reason as in the second stage. Thus the influence of altered geometry is realised by changing the vertical projected area, which is y_0 in this stage and has been incorporated in the prediction for f_l via the melting rate ratio (3.17).

In the derivation, the melting interface position is simplified as the average thickness of the melted liquid layer (s). This simplification removes the effect of interface curvature in the second and third stages, but its influence on the f_l solution is negligible. This is because the interface distortion does not change the vertical projected area of solid PCM and influences only rather trivially the average input heat flux in the melting thermal flow, compared with that in the pure thermal flow, as shown in figure 3(f).

4.2. *Parameter space and 3-D effect*

In this study, (3.8) is the central equation in the modelling, relating the average thickness of the melted liquid layer to the average thickness of the TBL, which is obtained by normalising the energy equation (2.3) at a low Stefan number (the upper limit $Ste \leq 0.3$ is deduced with an allowable error of $E_r < 10\%$ *a posteriori*). Then the solutions of f_l in the first and second stages are solved directly from (3.8), with the average TBL thickness (δ_T) determined from the scaling law of Nu in a laminar flow regime, which is derived and validated in the range $10^5 \leq Ra \leq 10^{10}$ by Shishkina (2016). In the third stage, f_l cannot be solved by (3.8) due to the leaking energy, which instead is modelled by establishing the relation of melting rate between the second and third stages (see (3.17)), where no extra restrictive condition is introduced. Thus the parameter space to which the predictions in this study are applicable corresponds to a laminar melting process with $Ra \leq 10^{10}$ and $Ste \leq 0.3$. This parameter space is consistent with the existing studies (Ho & Viskanta 1984; Bénard *et al.* 1985; Gau & Viskanta 1986; Webb & Viskanta 1986; Brent *et al.* 1988; Jany & Bejan 1988; Wolff & Viskanta 1988; Wang *et al.* 1999; Chakraborty & Chatterjee 2007; Huang *et al.* 2013; Luo *et al.* 2015; Duan *et al.* 2019), which also focus on the laminar melting process, since the PCM container in the engineering applications is usually small, indicating a low Rayleigh number.

In this study, the modelling is conducted in a 2-D situation, while the predictions are also applicable to 3-D cases. In the existing numerical studies, 3-D experimental data have been reproduced successfully by various 2-D laminar computational models (Webb & Viskanta 1986; Brent *et al.* 1988; Chakraborty & Chatterjee 2007; Duan *et al.* 2019; Rakotondrandisa *et al.* 2019). For example, Brent *et al.* (1988) and Chakraborty & Chatterjee (2007) both performed 2-D numerical simulations on the melting of gallium, predicting the 3-D experimental data by Gau & Viskanta (1986). As shown in figure 5(c), an overall agreement is achieved, and the acceptable error is attributed to the composite result of 3-D effects, experimental uncertainties and unaccounted variations in thermo-fluid properties (Chakraborty & Chatterjee 2007), indicating that the 3-D effects will not affect the melting process significantly. Moreover, in the existing experimental studies, Ho & Viskanta (1984), Bénard *et al.* (1985) and Wolff & Viskanta (1988) performed a series of 2-D and laminar simulations, and obtained quite good numerical predictions against their experimental data. Thus it is reasonable to conclude that the difference between 3-D and 2-D melting processes is trivial in the laminar regime. This is in line with expectations due to the absence of a 3-D turbulent vortex. Therefore, the predictions in the present study agree with the 3-D experimental data and the 2-D simulation results, as shown in figure 5.

4.3. *Transitions between two successive stages*

As in (3.23), the transition from the first to the second stage is determined by $f_l \leq 2k\,Ra^m\,Pr^n/\gamma$. Therefore, a decreasing γ would prolong the first stage and delay the transition, which explains the observation of Hamad *et al.* (2021) that an increasing cavity width (L_x), i.e. increasing γ, results in an early transition from first to second melting stages. Furthermore, setting $f_l = 2k\,Ra^m\,Pr^n/\gamma = 1$ leads to a critical Rayleigh number

$$Ra_c = \left(\frac{\gamma}{2k\,Pr^n}\right)^{1/m},\tag{4.1}$$

below which the melting process is always dominated by conduction, and no transition will occur.

The transition from the second to the third stage is characterised by f_l^c (see (3.21)). It is in a complicated mathematical form, and deriving a simple and convenient critical Rayleigh number to help avoid the third stage is difficult. However, this transition could still provide some instructions to optimise the latent heat system. For example, for a given operation condition with preset Ra and Pr, the aspect ratio of cavity (γ) can be determined numerically by imposing $f_l^c = 1$ to shorten the third stage and thus reduce the energy leakage.

5. Conclusions

The PCM melting problem is revisited in this paper in order to derive a full prediction of the melted liquid fraction for the entire melting process. In contrast to the commonly known traditional conduction–convection two-stage model, a three-stage model, where a third 'decaying convection' stage is recognised in the last part of the melting process, is more reasonable. In the third stage included in the present study, the leaking energy is considered quantitatively, and the continuously decreasing melting rate is explained directly. Based on this three-stage description, the melted liquid fraction f_l is derived analytically piecewise. The piecewise solution naturally includes the effects of all dimensionless control parameters (Ra, Pr, Ste and γ), and is able to predict reported results available in the literature, even though these results lead to different fitting correlations as summarised in table 1.

The prediction developed in this study applies to a laminar melting process, and the corresponding parameter space reads $Ra \leq 10^{10}$ and $Ste \leq 0.3$, covering the PCM melting in industrial processes. However, the present solution is inapplicable to the water–ice melting, because a density anomaly, in which the water density undergoes a maximum at $4\,^\circ$C and cannot be regarded as a constant, exists in this process. This anomaly is unique to water (Kamkari *et al.* 2014), and has been reported to affect significantly the water–ice melting behaviour (Z. Wang *et al.* 2021*a*,*b*,*c*). Thus the influence of this anomaly on the f_l solution needs further investigation. Other research directions should include the sub-cooling and cavity inclination effects, which are commonly encountered in practical applications.

Declaration of interests. The authors report no conflict of interest.

Data availability statement. The data that support the findings of this study are available from the authors on request.

Author ORCIDs.

Ⓘ Pan Jia https://orcid.org/0000-0002-3988-4363.

REFERENCES

AHMAD, M., BONTEMPS, A., SALLÉE, H. & QUENARD, D. 2006 Experimental investigation and computer simulation of thermal behaviour of wallboards containing a phase change material. *Energy Build.* **38** (4), 357–366.

ALBOUSSIERE, T., DEGUEN, R. & MELZANI, M. 2010 Melting-induced stratification above the Earth's inner core due to convective translation. *Nature* **466** (7307), 744–747.

BABY, R. & BALAJI, C. 2013 Experimental investigations on thermal performance enhancement and effect of orientation on porous matrix filled PCM based heat sink. *Intl Commun. Heat Mass Transfer* **46**, 27–30.

BAEHR, H.D. & STEPHAN, K. 2011 *Heat and Mass Transfer*. Springer Science & Business Media.

BAREISS, M & BEER, H 1984 Experimental investigation of melting heat transfer with regard to different geometric arrangements. *Intl Commun. Heat Mass Transfer* **11** (4), 323–333.

BEHBAHAN, A.S., NOGHREHABADI, A., WONG, C.P., POP, I. & BEHBAHANI-NEJAD, M. 2019 Investigation of enclosure aspect ratio effects on melting heat transfer characteristics of metal foam/phase change material composites. *Intl J. Numer. Meth. Heat Fluid Flow* **29**, 2994–3011.

BELMONTE, A., TILGNER, A. & LIBCHABER, A. 1994 Temperature and velocity boundary layers in turbulent convection. *Phys. Rev.* E **50** (1), 269.

BÉNARD, C, GOBIN, D & MARTINEZ, F 1985 Melting in rectangular enclosures: experiments and numerical simulations. *Trans. ASME: J. Heat Transfer* **107** (4), 794–803.

BERTRAND, O., *et al.* 1999 Melting driven by natural convection a comparison exercise: first results. *Intl J. Therm. Sci.* **38** (1), 5–26.

BOGER, D.V. & WESTWATER, J.W. 1967 Effect of buoyancy on the melting and freezing process. *J. Heat Transfer* **89** (1), 81–89.

BRENT, A.D., VOLLER, V.R & REID, K.T.J 1988 Enthalpy-porosity technique for modeling convection–diffusion phase change: application to the melting of a pure metal. *Numer. Heat Transfer,* A *Applics* **13** (3), 297–318.

CAMPBELL, T.A. & KOSTER, J.N. 1994 Visualization of liquid–solid interface morphologies in gallium subject to natural convection. *J. Cryst. Growth* **140** (3-4), 414–425.

CHAKRABORTY, S. & CHATTERJEE, D. 2007 An enthalpy-based hybrid lattice-Boltzmann method for modelling solid–liquid phase transition in the presence of convective transport. *J. Fluid Mech.* **592**, 155–175.

DHAIDAN, N.S & KHODADADI, J.M. 2015 Melting and convection of phase change materials in different shape containers: a review. *Renew. Sustain. Energy Rev.* **43**, 449–477.

DU, Y., YUAN, Y., JIA, D., CHENG, B. & MAO, J. 2007 Experimental investigation on melting characteristics of ethanolamine–water binary mixture used as PCM. *Intl Commun. Heat Mass Transfer* **34** (9–10), 1056–1063.

DUAN, J., XIONG, Y. & YANG, D. 2019 On the melting process of the phase change material in horizontal rectangular enclosures. *Energies* **12** (16), 3100.

DUTIL, Y., ROUSSE, D.R., SALAH, N.B., LASSUE, S. & ZALEWSKI, L. 2011 A review on phase-change materials: mathematical modeling and simulations. *Renew. Sustain. Energy Rev.* **15** (1), 112–130.

EL QARNIA, H, DRAOUI, A & LAKHAL, E.K. 2013 Computation of melting with natural convection inside a rectangular enclosure heated by discrete protruding heat sources. *Appl. Math. Model.* **37** (6), 3968–3981.

ESFAHANI, B.R., HIRATA, S.C, BERTI, S. & CALZAVARINI, E. 2018 Basal melting driven by turbulent thermal convection. *Phys. Rev. Fluids* **3** (5), 053501.

FADEN, M., LINHARDT, C., HÖHLEIN, S., KÖNIG-HAAGEN, A. & BRÜGGEMANN, D. 2019 Velocity field and phase boundary measurements during melting of n-octadecane in a cubical test cell. *Intl J. Heat Mass Transfer* **135**, 104–114.

FAVIER, B., PURSEED, J. & DUCHEMIN, L. 2019 Rayleigh–Bénard convection with a melting boundary. *J. Fluid Mech.* **858**, 437–473.

GADGIL, A & GOBIN, D 1984 Analysis of two-dimensional melting in rectangular enclosures in presence of convection. *Trans. ASME: J. Heat Transfer* **106** (1), 20–26.

GARG, H.P., MULLICK, S.C. & BHARGAVA, V.K 2012 *Solar Thermal Energy Storage*. Springer Science & Business Media.

GAU, C & VISKANTA, R 1985 Effect of natural convection on solidification from above and melting from below of a pure metal. *Intl J. Heat Mass Transfer* **28** (3), 573–587.

GAU, C. & VISKANTA, R 1986 Melting and solidification of a pure metal on a vertical wall. *Trans. ASME: J. Heat Transfer* **108** (1), 174–181.

GONG, Z.-X., DEVAHASTIN, S. & MUJUMDAR, A.S 1999 Enhanced heat transfer in free convection-dominated melting in a rectangular cavity with an isothermal vertical wall. *Appl. Therm. Engng* **19** (12), 1237–1251.

HAMDAN, M.A & AL-HINTI, I. 2004 Analysis of heat transfer during the melting of a phase-change material. *Appl. Therm. Engng* **24** (13), 1935–1944.

HAMAD, F.A., EGELLE, E., CUMMINGS, K. & RUSSELL, P. 2017 Investigation of the melting process of polyethylene glycol 1500 (PEG 1500) in a rectagular enclosure. *Intl J. Heat Mass Transfer* **114**, 1234–1247.

HAMAD, F.A., EGELLE, E., GOONERATNE, S. & RUSSELL, P. 2021 The effect of aspect ratio on PCM melting behaviour in rectangular enclosure. *Intl J. Sustain. Engng* **14** (5), 1251–1268.

HAMDAN, M.A. & ELWERR, F.A. 1996 Thermal energy storage using a phase change material. *Solar Energy* **56** (2), 183–189.

HANNOUN, N., ALEXIADES, V. & MAI, T.Z. 2003 Resolving the controversy over tin and gallium melting in a rectangular cavity heated from the side. *Numer. Heat Transfer:* B*: Fundam.* **44** (3), 253–276.

HASAN, M.S. & SAHA, S.K 2021 Evolution of solid–liquid interface in bottom heated cavity for low Prandtl number using lattice Boltzmann method. *Phys. Fluids* **33** (5), 057102.

HE, Y., QI, C., HU, Y., QIN, B., LI, F. & DING, Y. 2011 Lattice Boltzmann simulation of alumina–water nanofluid in a square cavity. *Nanoscale Res. Lett.* **6** (1), 184.

HO, C-J & VISKANTA, R 1984 Heat transfer during melting from an isothermal vertical wall. *Trans. ASME: J. Heat Transfer* **106** (1), 12–19.

HUANG, R., WU, H. & CHENG, P. 2013 A new lattice Boltzmann model for solid–liquid phase change. *Intl J. Heat Mass Transfer* **59**, 295–301.

JANY, P. & BEJAN, A. 1988 Scaling theory of melting with natural convection in an enclosure. *Intl J. Heat Mass Transfer* **31** (6), 1221–1235.

JOURABIAN, M., FARHADI, M. & DARZI, A.A.R. 2013 Convection-dominated melting of phase change material in partially heated cavity: lattice Boltzmann study. *Heat Mass Transfer* **49** (4), 555–565.

KADRI, S., DHIFAOUI, B., DUTIL, Y., JABRALLAH, S.B. & ROUSSE, D.R 2015 Large-scale experimental study of a phase change material: shape identification for the solid–liquid interface. *Intl J. Thermophys.* **36** (10), 2897–2915.

KAKAC, S., AUNG, W. & VISKANTA, R. 1985 *Natural Convection: Fundamentals and Applications.* Hemisphere.

KAMKARI, B., SHOKOUHMAND, H. & BRUNO, F. 2014 Experimental investigation of the effect of inclination angle on convection-driven melting of phase change material in a rectangular enclosure. *Intl J. Heat Mass Transfer* **72**, 186–200.

KIM, T.Y., HYUN, B.-S., LEE, J.-J. & RHEE, J. 2013 Numerical study of the spacecraft thermal control hardware combining solid–liquid phase change material and a heat pipe. *Aerospace Sci. Technol.* **27** (1), 10–16.

KIM, M.C., LEE, D.W. & CHOI, C.K. 2008 Onset of buoyancy-driven convection in melting from below. *Korean J. Chem. Engng* **25** (6), 1239–1244.

LEE, K.O., MEDINA, M.A, RAITH, E. & SUN, X. 2015 Assessing the integration of a thin phase change material (PCM) layer in a residential building wall for heat transfer reduction and management. *Appl. Energy* **137**, 699–706.

LEVIN, P.P, SHITZER, A. & HETSRONI, G. 2013 Numerical optimization of a PCM-based heat sink with internal fins. *Intl J. Heat Mass Transfer* **61**, 638–645.

LI, Z., YANG, M. & ZHANG, Y. 2014 A hybrid lattice Boltzmann and finite-volume method for melting with convection. *Numer. Heat Transfer,* B*: Fundam.* **66** (4), 307–325.

LUO, K., YAO, F.-J., YI, H.-L. & TAN, H.-P. 2015 Lattice Boltzmann simulation of convection melting in complex heat storage systems filled with phase change materials. *Appl. Therm. Engng* **86**, 238–250.

NAZIR, H., BATOOL, M., OSORIO, F.J.B.olivar, ISAZA-RUIZ, M., XU, X., VIGNAROOBAN, K, PHELAN, P., KANNAN, A.M, *et al.* 2019 Recent developments in phase change materials for energy storage applications: a review. *Intl J. Heat Mass Transfer* **129**, 491–523.

NG, C.S., OOI, A., LOHSE, D. & CHUNG, D. 2015 Vertical natural convection: application of the unifying theory of thermal convection. *J. Fluid Mech.* **764**, 349–361.

PURSEED, J., FAVIER, B., DUCHEMIN, L. & HESTER, E.W 2020 Bistability in Rayleigh–Bénard convection with a melting boundary. *Phys. Rev. Fluids* **5** (2), 023501.

RAKOTONDRANDISA, A., DANAILA, I. & DANAILA, L. 2019 Numerical modelling of a melting-solidification cycle of a phase-change material with complete or partial melting. *Intl J. Heat Fluid Flow* **76**, 57–71.

RAMAKRISHNAN, S., WANG, X., ALAM, M., SANJAYAN, J. & WILSON, J. 2016 Parametric analysis for performance enhancement of phase change materials in naturally ventilated buildings. *Energy Build.* **124**, 35–45.

RUI, Z., LI, J., MA, J., CAI, H., NIE, B. & PENG, H. 2020 Comparative study on natural convection melting in square cavity using lattice Boltzmann method. *Results Phys.* **18**, 103274.

SARIER, N. & ONDER, E. 2012 Organic phase change materials and their textile applications: an overview. *Thermochim. Acta* **540**, 7–60.

SCHEEL, J.D & SCHUMACHER, JÖRG 2014 Local boundary layer scales in turbulent Rayleigh–Bénard convection. *J. Fluid Mech.* **758**, 344–373.

SHARIFI, N., ROBAK, C.W, BERGMAN, T.L & FAGHRI, A. 2013 Three-dimensional PCM melting in a vertical cylindrical enclosure including the effects of tilting. *Intl J. Heat Mass Transfer* **65**, 798–806.

SHARMA, A., TYAGI, V.V., CHEN, C.R. & BUDDHI, D. 2009 Review on thermal energy storage with phase change materials and applications. *Renew. Sustain. Energy Rev.* **13** (2), 318–345.

SHISHKINA, O. 2016 Momentum and heat transport scalings in laminar vertical convection. *Phys. Rev.* E **93** (5), 051102.

SHOKOUHMAND, H. & KAMKARI, B. 2013 Experimental investigation on melting heat transfer characteristics of lauric acid in a rectangular thermal storage unit. *Exp. Therm. Fluid Sci.* **50**, 201–212.

SWANSON, T.D & BIRUR, G.C 2003 NASA thermal control technologies for robotic spacecraft. *Appl. Therm. Engng* **23** (9), 1055–1065.

TAKESHITA, T., SEGAWA, T., GLAZIER, J.A & SANO, M. 1996 Thermal turbulence in mercury. *Phys. Rev. Lett.* **76** (9), 1465.

VERZICCO, R & CAMUSSI, R 1999 Prandtl number effects in convective turbulence. *J. Fluid Mech.* **383**, 55–73.

WANG, Q., LIU, H.-R., VERZICCO, R., SHISHKINA, O. & LOHSE, D. 2021 Regime transitions in thermally driven high-Rayleigh number vertical convection. *J. Fluid Mech.* **917**, A6.

WANG, S., FAGHRI, A. & BERGMAN, T.L 2010 A comprehensive numerical model for melting with natural convection. *Intl J. Heat Mass Transfer* **53** (9-10), 1986–2000.

WANG, Y, AMIRI, A & VAFAI, K 1999 An experimental investigation of the melting process in a rectangular enclosure. *Intl J. Heat Mass Transfer* **42** (19), 3659–3672.

WANG, Z., CALZAVARINI, E. & SUN, C. 2021*a* Equilibrium states of the ice–water front in a differentially heated rectangular cell (a). *Europhys. Lett.* **135** (5), 54001.

WANG, Z., CALZAVARINI, E., SUN, C. & TOSCHI, F. 2021*b* How the growth of ice depends on the fluid dynamics underneath. *Proc. Natl Acad. Sci.* **118** (10), e2012870118.

WANG, Z., JIANG, L., DU, Y., SUN, C. & CALZAVARINI, E. 2021*c* Ice front shaping by upward convective current. *Phys. Rev. Fluids* **6** (9), L091501.

WEBB, B.W. & VISKANTA, R 1986 Analysis of heat transfer during melting of a pure metal from an isothermal vertical wall. *Numer. Heat Transfer,* A*: Applics.* **9** (5), 539–558.

WOLFF, F & VISKANTA, R 1988 Solidification of a pure metal at a vertical wall in the presence of liquid superheat. *Intl J. Heat Mass Transfer* **31** (8), 1735–1744.

YANG, X., GUO, Z., LIU, Y., JIN, L. & HE, Y.-L. 2019 Effect of inclination on the thermal response of composite phase change materials for thermal energy storage. *Appl. Energy* **238**, 22–33.

ZHANG, Y., CHEN, Z., WANG, Q. & WU, Q. 1993 Melting in an enclosure with discrete heating at a constant rate. *Exp. Therm. Fluid Sci.* **6** (2), 196–201.

ZHOU, Q., STEVENS, R.J.A.M, SUGIYAMA, K., GROSSMANN, S., LOHSE, D. & XIA, K.-Q. 2010 Prandtl–Blasius temperature and velocity boundary-layer profiles in turbulent Rayleigh–Bénard convection. *J. Fluid Mech.* **664**, 297–312.

ZHOU, Q. & XIA, K.-Q. 2010 Measured instantaneous viscous boundary layer in turbulent Rayleigh–Bénard convection. *Phys. Rev. Lett.* **104** (10), 104301.

ZHOU, D., ZHAO, C.-Y. & TIAN, Y. 2012 Review on thermal energy storage with phase change materials (PCMs) in building applications. *Appl. Energy* **92**, 593–605.